Resonance-mediated atomic ionization dynamics induced by ultraintense x-ray pulses

Phay J. Ho, E. P. Kanter, and L. Young

Phys. Rev. A **92**, 063430 — Published 31 December 2015

DOI: 10.1103/PhysRevA.92.063430

Resonance-mediated Atomic Ionization Dynamics Induced by Ultraintense X-ray Pulses

Phay J. Ho, E. P. Kanter, and L. Young
Argonne National Laboratory, Argonne, Illinois 60439, USA

We describe the methodology of our recently developed Monte-Carlo rate equation (MCRE) approach, which, for the first time, systematically incorporates bound-bound resonances to model multiphoton ionization dynamics induced by high-fluence, high-intensity x-ray free electron laser (XFEL) pulses. These resonances are responsible for ionization *far* beyond that predicted by the sequential single photon absorption model and are central to a quantitative understanding of atomic ionization dynamics in XFEL pulses. We also present calculated multiphoton ionization dynamics for Kr and Xe atoms in XFEL pulses for a variety of conditions, to compare the effects of bandwidth, pulse duration, pulse fluence and photon energy. This comprehensive computational investigation reveals areas in the photon energy - pulse fluence landscape where resonances are critically important. We also uncover a mechanism, preservation of inner-shell vacancies (PIVS), whereby radiation damage is enhanced at higher XFEL intensities and identify the sequence of core-outer/Rydberg, core-valence, and core-core resonances encountered during multiphoton x-ray ionization.

PACS numbers: 32.80.Rm, 41.60.Cr, 02.70.Uu

I. INTRODUCTION

X-ray free-electron laser (XFEL) pulses, as currently available at the Linac Coherent Light Source (LCLS) [1] and SPring-8 Angstrom Compact Free Electron Laser (SACLA) [2], represent an unprecedented tool to follow dynamics on femtosecond timescales and determine structure with Angstrom resolution. Since these pulses contain high photon number, multiphoton interaction is almost unavoidable in the focused beam [3–7]. Indeed the first experiment at LCLS found that all ten electrons could be stripped from a neon atom in a single 100-femtosecond x-ray pulse [3]. This implies that during the course of a single ultrashort pulse the absorption spectrum and the scattering power of all atoms exposed to the x-ray beam are changing, and that x-ray snapshots derived from a single pulse are not representative of the initial state, but rather an evolving x-ray driven sample. Thus, it is of fundamental interest to understand the electron dynamics within the sample for any application, most notably for single particle imaging and serial femtosecond crystallography where ultraintense focused x-ray pulses are required [8–10].

The characteristics of XFEL pulses along with atomic structure properties dictate the induced electron dynamics within atoms. Initially XFELs operated in the SASE (Self-Amplified Spontaneous Emission) mode [11] and produced chaotic pulses with relatively large bandwidth and jitter approaching 1% of the photon energy. More recently researchers have been actively pursuing developments beyond the SASE mode. Using novel self-seeding schemes [12, 13], narrow bandwidth XFEL pulses in both the hard x-ray [14] and soft x-ray [15] regime were produced. The seeded mode leads to dramatic improvement in wavelength stability and, in comparison to the SASE mode, has a much narrower bandwidth of the order of 0.01% of the x-ray photon energy. In addition, seeding is expected to provide a means to significantly higher XFEL intensities to the 10-terawatt level [16]. Developments are also underway to improve pulse stability and add novel features to the seeded pulse operation mode, such as two-color femtosecond pulses [15, 17, 18]. These new capabilities further motivate detailed understanding of the fundamental interactions of XFEL pulses with atoms and molecules as they can impact potential applications such as following chemical dynamics in real time, performing structural analysis of complex materials and controlling inner-shell processes in atoms and molecules and complex materials.

In this paper we follow our recent publication [19] where we reported a Monte Carlo rate equation (MCRE) approach to track electron dynamics in XFEL-irradiated atoms which included, for the first time, bound-bound resonance transitions. In that work, we provided the first theoretical validation of the Resonance-Enhanced X-Ray Multiple Ionization (REXMI) mechanism which enables efficient production of unexpectedly high charge states observed in XFEL studies of atomic ionization of Ar at 0.48 keV [20, 21], Kr at 2.0 keV [7] and Xe at 1.5 keV [6]. We predicted the striking observation for Xe irradiated with 1.5 keV XFEL pulses of charge states up to 36+, far beyond the sequential single photon limit of 26+. Simpler MCRE codes that do not include resonances used for XFEL interactions, e.g. XATOM [22–24], fail to predict the REXMI mechanism. Previously, MCRE simulations have been employed to model vacancy cascades initiated from a single inner-shell ionization event as observed in synchrotron studies [25–30]. The MCRE method was then adapted by Son and co-workers [24] to investigate the response of Xe [5, 6, 31], Kr [7] and Ar [31] atoms to XFEL pulses. The computational challenge to include bound-bound transitions is extreme, but critical to master, as resonances play an important role in understanding differences between seeded and SASE pulses. Here we present details of the advances in MCRE methodol-

ogy and new predictions for Kr and Xe under a variety of XFEL-pulse conditions.

In ultraintense XFEL interactions with atoms, the dominant mechanism is sequential single photon ionization up to a maximal charge state where one-photon ionization is no longer energetically allowed. This was firmly established as the dominant ionization mechanism for x-ray intensities approaching 10^{18}W/cm^2 [3] in accordance with earlier theoretical predictions [32]. Although these intensities appear extreme, nonsequential two-photon absorption was found to be relatively weak [33], though stronger than simple theoretical predictions - a finding which could be reconciled by invoking the presence of nearby resonances [34]. Nevertheless, even in this case when resonances are not included, the computational requirements are large for systems containing many electrons [24]. Why? If only one photon is absorbed, as in synchrotron studies, creating an inner-shell hole, Auger relaxation produces multiply charged ions, but only a handful of transients are involved. However in an ultraintense XFEL pulse, photoabsorption rates are comparable to the inner-shell relaxation rates and can interrupt the inner-shell cascade. Thus, an XFEL pulse produces a different and larger set of intermediate transients compared to a synchrotron pulse.

Resonances can greatly alter the basic ionization process. Resonance behavior in XFEL pulses was investigated early by Kanter and coworkers [35]. Here the leading edge of the XFEL pulse was used to reveal a 'hidden" resonance in neon by creating a 2p hole and, with the photon energy tuned properly, the $1s-2p$ transition could be Rabi-cycled. Resonances have cross sections that are several orders of magnitude higher than the underlying background continuum. The general scenario for hidden resonance effects is that the pulse opens windows for resonance excitations (REs) that eventually terminate as the charge state increases.

This paper is organized as follows. In Section 2, the Monte Carlo rate equation and our numerical implementation that allows for the study of resonant phenomena is discussed. In Sections 3 and 4, the calculated ionization dynamics of Kr and Xe atoms are presented. Finally, a summary of our results is presented in Section 5.

II. SECTION 2: THEORETICAL METHOD AND IMPLEMENTATION

The time-dependent population of an electronic configuration (EC) $\mathbf{N}^{(J)}$ of an atom produced in its interaction with an intense x-ray pulse can be modeled using the rate equation [3, 36]

$$\frac{dP_{\mathbf{N}^{(J)}}(t)}{dt} = \gamma(t) P_{\mathbf{N}^{(J)}}(t) \tag{1}$$

where $P_{\mathbf{N}^{(J)}}(t)$ is a vector that contains the population of all ECs, $\gamma(t)$ is a matrix containing all the transition rates and $\mathbf{N}^{(J)} = \{N_1^{(J)}, N_2^{(J)}, ..., N_M^{(J)}\}$ gives a set of occupation numbers in M subshells. Here, J is the label of this EC and $N_i^{(J)}$ is the number of electrons occupying the i subshell.

	# of ECs with no RE	# of ECs with RE
He	3	861
Ne	63	9.65×10^9
Ar	1.33×10^3	3.40×10^{14}
Kr	3.05×10^5	1.85×10^{21}
Xe	7.06×10^7	4.65×10^{25}

TABLE I. Number of possible ECs for rare-gas atom calculations if resonant excitation (RE) is excluded and if RE is included up to 10 g orbitals. These numbers are calculated using the equation given in [37].

For systems with a small number of electrons and no resonant transition, the direct integration method for solving eq. (1) can be convenient and manageable [3, 36]. But, for heavy elements, which have a large number of ECs, this integration method becomes very inefficient. In the case that resonant transitions are included, implementation of that method is impossible. This is because that method requires a small time step to capture the fastest electronic transition (∼attoseconds) and a long timescale to describe the relaxation processes, which can be picoseconds or longer, when an accurate final ion count is desired. A more demanding aspect is the computation of the transition rate matrix for all ECs. Since the importance of individual ECs is not known *a priori*, all ECs would need to be included.

The challenge of solving the rate equation via direct numerical integration is illustrated in Table I which lists the numbers of ECs with and without inclusion of REs. Here the number of ECs are counted up to the Rydberg state of 10 g, an increment of 2 in l and 5 in n over occupied ECs in ground state Xe, and consisting of a set of 40 subshells. For Xe, the number of ECs is increased by more than 15 orders of magnitude if RE is included. Merely storing the population of each EC is computationally challenging. This set of subshells is found to be sufficient to account for the Xe and Kr ionization dynamics and give a converged ion yield value with a precision of 0.01% for our chosen range of XFEL pulse parameter sets. For different pulse parameters and precision, different ranges of n and l quantum number might be needed.

Thus, the Monte Carlo rate equation (MCRE) method, which can efficiently and dynamically select the most probable ECs, is a logical choice for studies involving heavy elements [24] and resonant phenomena [19]. Briefly, an ensemble of atoms with the same starting electronic configuration of $\mathbf{N}^{(J_0)}$ is tracked throughout an XFEL pulse starting at t_0. Essentially their individual response is recorded as a time sequence of ECs:

$$\mathbf{N}^{(J_0)} \xrightarrow{t_1} \mathbf{N}^{(J_1)} \xrightarrow{t_2} ...\mathbf{N}^{(J_{k-1})} \xrightarrow{t_k} \mathbf{N}^{(J_k)}. \tag{2}$$

At each time step, a random number is generated to determine whether an electronic transition will take

place. Possible electronic transitions include, photoionization, resonant absorption, Auger, Coster-Kronig, auto-ionization and fluorescence. The probability of a transition being selected is weighted by its transition strength, which is its transition rate multiplied by the chosen time step size. If an electronic transition occurs at t_1, the atom will have a new electronic configuration of $\mathbf{N}^{(J_1)}$. This procedure is then repeated for $\mathbf{N}^{(J_1)}$ until the atom reaches a final EC of $\mathbf{N}^{(J_k)}$, which has no more decay channels. For our ensemble of atoms, the individual time sequences can vary from each other. Collectively, they are used to construct the time-dependent probability of each EC, which is the solution of eq. (1), and various observables, like the ion yield and statistical data of each type of electronic transition. Since each electronic transition is treated as an independent, random event, an adaptive time stepping approach is usually used to speed up the computation.

The atomic data of all needed electronic configurations (ECs) are computed using the Hartree-Fock-Slater model [38–40]. Following the treatment in [23, 40–51], we calculate the bound-state and continuum orbital wave functions, orbital energies, photoionization and resonant absorption cross section, Auger, Coster-Kronig, autoionization and fluorescence rates. We use a variant of the Herman-Skillman code, with a different numerical grid based on the pseudo-spectral method [52–56] to describe the bound states. This grid method provides flexible and optimal numerical grid, dense near the nucleus and sparse away from the nucleus, for better control of convergence and stability. Continuum states are decribed by a dense uniform grid. Our method is similar to those used in the XATOM toolkit [22–24].

A. 2a: Database

A critical element that enables inclusion of resonant excitations in MCRE is database design with a unique labelling scheme for each encountered EC. A convenient way to assign a unique integral ID to an EC, $\mathbf{N}^{(J)}$, with occupation number N_i as

$$\mathscr{J} = \sum_{i=1}^{M} N_i^{(J)} f_i \tag{3}$$

$$f_i = \sum_{j=2}^{i} f_{j-1}(g_j + 1); \quad f_1 = 1; \tag{4}$$

where g_j is the maximum occupancy of the subshell j, adding and removing an electron from the j-th shell changes the index by a value of f_j. The value $\mathscr{J}$, then, can be used to provide a direct mapping to the location of desired atomic data in the database. However, when excitation is included, such a mapping scheme will not work because $\mathscr{J}$ can be larger than the maximum value of a 64-bit integer, $2^{64} - 1$.

Thus, we designed a search-based mechanism to access the database. For each run, we first setup a database by storing the atomic data of all the known ECs from an input file. The atomic data are collected from previous related calculations. Each entry of atomic data of an EC has a numeral index, which merely labels the order that this EC is stored in the database. So, the largest index corresponds to the number of ECs stored in the database. In order to shorten the query time, our database has an EC key generator (ECKG) and active EC array (AECA). The function of ECKG is to generate a unique key for a particular EC, which is an M-character string with each character encoding the occupation number of each subshell. For example, the EC of Xe^+ with two 2p holes and an electron in 7d" has a unique key of "c ce cgk cgka cgaaa aaaaa aabaa aaaaa aaaaa aaaaa" with the characters a, b, c, ... and k representing an occupancy number of 0, 1, 2, ..., 10 respectively. The spaces in the key are added for clarity to separate groups of subshells with increasing n values, and the subshells are arranged in the order of increasing l values. The AECA is an associative array, which is an abstract data type composed of a collection of (key, index, frequency) triples. The index points to the index of entry of atomic data of the given EC. This AECA contains only ECs that have been invoked in this run. Thus, the number of entries is usually much smaller than the number of the ECs stored in the database. With this array, we can reduce the query time.

At each time step, when an electronic transition takes place leading to a new EC, we generate a key for this new EC using ECKG. Next we search AECA to find out if this new EC has been invoked before by comparing its key with the entries of AECA sequentially. When the desired key matches one of those in the AECA, the corresponding index would point to the atomic data of the desired EC in the database and the frequency counter will be increased by 1. Note that this array is sorted regularly throughout the calculation based on the frequencies of individual ECs encountered while the order of the database remains unchanged. To further speed up the search process, the active EC array can be decomposed into many subsets based on ion charge state and number of excited electrons.

If the AECA does not contain this EC, we proceed to search the database sequentially. If the entry is found in the database, AECA will be updated and the atomic data of this EC can be retrieved for calculation. However, in the case that this EC is also absent in the database, the atomic data of this EC will be generated and both the AECA and the database will be updated. In this way, the size of the database and the AECA expands as more atoms are calculated. Of course, the number of the important ECs depends strongly on the pulse parameters; it will grow with higher photon fluence and larger bandwidth. But, for all the calculations presented, the number of important ECs, which ranges from tens of thousands for Kr and hundreds of thousands for Xe, is still manageable using a personal computer. At the end of each run, this database is output to a file, which can be read as an input and further expanded in future calculations.

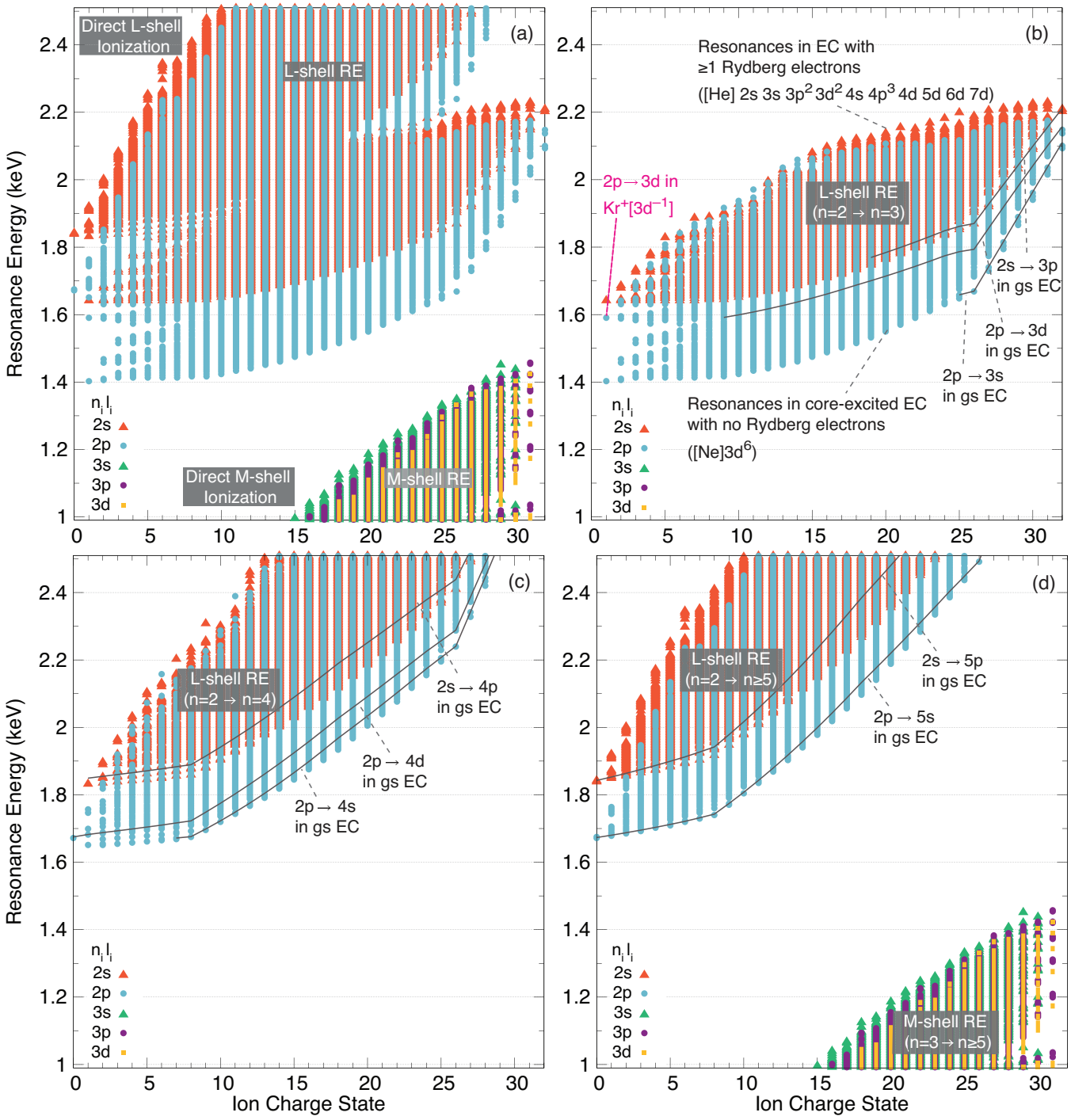

FIG. 1. (Color online) (a) The resonance landscape for various charge states of Kr that can be uncovered over a range of incoming x-ray photon energies. The resonances in this scatter plot are separated into 5 groups depending on the initial subshell. The red triangles, blue circles, green triangles, purple circles and yellow squares designate the resonances from $2s$, $2p$, $3s$, $3p$ and $3d$ subshell respectively. Panel (b), (c) and (d) show only the resonances to $n = 3$ (core shell), $n = 4$ (valence shell) and $n \geq 5$ (outer or Rydberg shell) respectively. Each solid curve traces a series of the same type resonance transition, like $2p \rightarrow 3s$, in ground state EC as a function of ion charge state. We note that some of these transitions in ions with ground-state EC are not allowed due to the lack of the vacancy in the upper subshells. For example, there is no $2p \rightarrow 3d$ in ground-state Kr^+, but this transition is found in an excited EC of $Kr^+[3d^{-1}]$ (highlighted in pink in (b)), which is responsible for an ultraefficient ionization in a 1.6-keV SASE pulse. The column-like appearances are due to the stacking of multiple resonances with similar energies. For example in (b), the highest and lowest energy $2p \rightarrow 3s$ in Kr^{20+} are 480 eV apart.

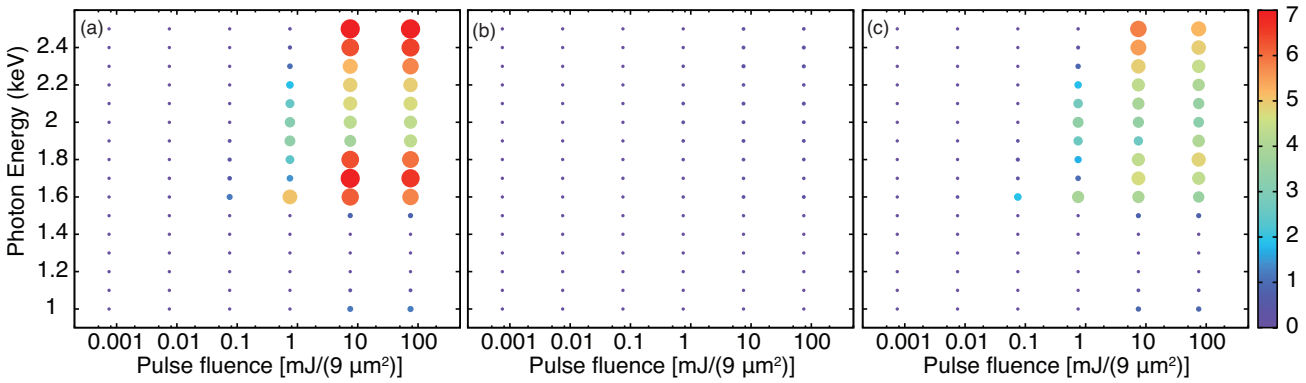

FIG. 2. (Color online) Average number of resonant excitation events (ANREE) occurred in producing a krypton ion in (a) an 80-fs, 1% BW XFEL pulse, (b) an 80-fs, 0.01% BW XFEL pulse, and (c) an 7-fs, 1% BW XFEL pulse as a function of x-ray photon energies and pulse energy (or fluence) with an x-ray focus of 9 μm^2. To enhance the visibility of its pulse energy and ω_X dependence, larger circles are used to indicate large ANREE in addition to the color-coded legend.

III. SECTION 3: KRYPTON IONIZATION DYNAMICS

Using the MCRE method, we examine the effects of pulse parameters (x-ray photon energy, pulse duration, fluence and bandwidth) on the ionization dynamics of Kr and Xe in an XFEL pulse. For each parameter set, 10,000 to 50,000 trajectories are used to obtain converged ion yield values.

We first present the Kr results calculated over a range of pulse parameters (photon energy 1.0 – 2.5 keV, pulse duration 7 – 80 fs, pulse energy 0.75 $\times 10^{-3}$ – 0.75×10^2 mJ). The parameter range spans the earlier Kr measurement performed with 80-fs SASE XFEL pulses at 1.5 and 2.0 keV with pulse energies between 0.3 to 0.5 mJ and a focal area of 9 μm^2 [7]. Our previous calculations [19], which include spatial intensity averaging, confirm that resonances are needed to reproduce experimental ion yields of Kr at 2.0 keV, but are not important at 1.5 keV. Here we extend our study over a larger range of pulse parameters to shed light on the photon-energy dependence of XFEL resonance physics. A significant motivation of this study is to understand the effect of bandwidth (SASE vs seeded mode) on ionization dynamics.

We computed the Kr atomic ionization dynamics for three different groups of XFEL pulses: 1) SASE pulse with energy bandwidth (BW) (1%), 80-fs duration, 2) seeded pulse BW (0.01%), 80-fs duration, 3) SASE pulse BW (1%), 7-fs duration. The 7-fs pulse duration is standard at SACLA [57]. For a given pulse energy (PE) and x-ray photon energy (ω_X), these three pulse groups contain the same photon number. For each group of pulses we calculated 16 ω_X values (1 to 2.5 keV) and 6 different PEs incremented by 10x (0.75×10^{-3} mJ – 0.75×10^2 mJ). Each pulse is assumed to have a flattop spatial profile and a focus of 9 μm^2, as used in the earlier measurement [7]. The PEs correspond to a pulse fluence of 0.00083 to 8.3 mJ/μm^2. The PEs span those currently available and anticipate future XFEL capabilities; 2×10^{13} photons/pulse for ω_X between 0.2-2 keV are available at LCLS At 1.0 (2.5) keV, our selected PEs correspond to a photon number of 4.68×10^9 – 4.68×10^{14} (1.87×10^9 –1.87×10^{14}) per pulse.

A. 3a: Energy Landscape of Hidden Resonances in Kr

For a given ω_X, many resonances can be encountered. Figure 1 shows the landscape of these resonances as a function of transition energy and charge state. To produce this landscape, we plot all dipole transitions from all electron configurations (ECs) encountered in our calculations, and select those transitions that have transition energies within the range 1 – 2.5 keV. The initial state ECs include ECs of the neutral atom and ground state and excited state ions.

Figure 1 distinguishes the initial subshell (n_i and l_i quantum numbers) of each transition with different symbols and colors, triangles for ns and filled circles for np etc. The charge state window where REs are relevant depend strongly on ω_X. For resonance energy $\geq$ 1.4 keV, REs are dominated by the L-shell excitations; $2p$ and $2s$ resonances begin at 1.4 keV and 1.6 keV, respectively. Below 1.4 keV, L-shell REs are largely absent, and M-shell REs are only found in charge states > 15.

We further separate the resonances from Figure 1(a) into three groups with different final states, $n_f = 3$, $n_f = 4$ and $n_f \geq 5$, in Figs. 1 (b), (c) and (d) respectively. For the Kr atom, REs with $n_f = 3$, $n_f = 4$ and $n_f \geq 5$ correspond to excitation to core, valence and unoccupied atomic shells respectively. We see that REs near and below 1.6 keV are mainly core-to-core transitions, whereas above 2.2 keV only REs with $n_f > 3$ are available. But, between 1.6 keV and 2.2 keV, a mixture of these three groups of REs with different n_f are found with significant overlap among them, in terms of their charge state window.

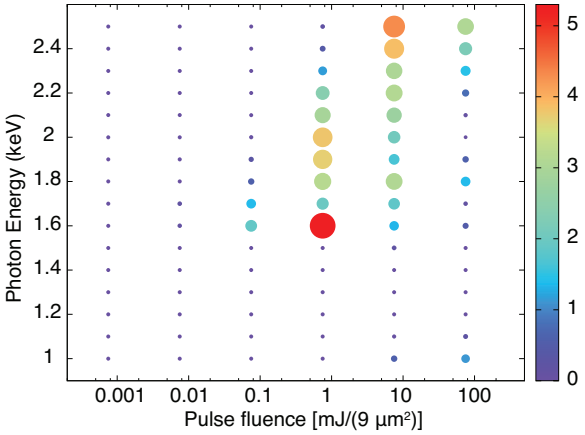

FIG. 3. (Color online) The difference signals between the average charge state of Kr ions exposed to a SASE pulse (BW = 1%) and a seeded pulse (BW = 0.01%) as a function of x-ray photon energies and pulse energy.

B. 3b: Resonant excitations: dependence on pulse duration and bandwidth

We characterize the role of resonant excitation for each set of pulse parameters by calculating the average number of resonant excitation events (ANREE), which is the sum of resonant excitations for each trajectory divided by the number of trajectories used. Large ANREE suggests that RE channels play an important role.

Figure 2(a) shows ANREE as a function of x-ray photon energy and pulse fluence for 80-fs pulses with 1% BW. ANREE correlates well with the availability of the RE channels shown in Fig. 1. ANREE is negligible for ω_X in the range of 1.0 to 1.4 keV since there are no REs

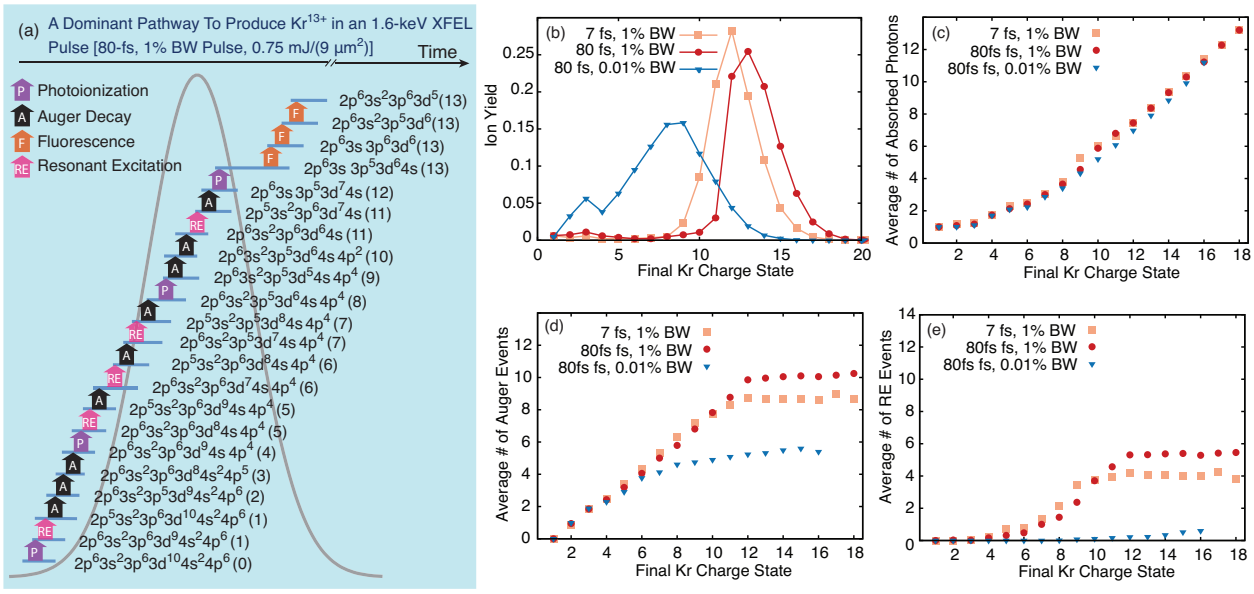

FIG. 4. (Color online) The ionization dynamics of Kr in three different 1.6-keV, 0.75-mJ pulses: 7-fs SASE pulse, 80-fs SASE pulse and 80-fs seeded pulse. (a) A dominant ionization pathway to Kr^{13+} with a series of REs. The number in each parenthesis after the electronic configuration indicates the associated ion charge state. (b) The ion yield, (c) the average number of absorbed photons, (d) the average number of Auger decays and (e) the average number of RE events of various final charge states.

or the available REs are hidden at very high charge state which are inaccessible unless very high fluence pulses are used. For pulses with photon energy higher than 1.4 keV, ANREE is found to increase with pulse fluence and can be as high as 7. Since excited transients have finite lifetime, a sufficiently high pulse fluence is needed to beat the transient decay to increase the chance of invoking REs. This strong dependence on pulse fluence suggests that SASE pulses have sufficiently large BW to activate multiple RE channels, each with slightly different transition energy.

With an 80-fs "seeded" pulse with 100-fold narrower BW than the SASE pulses, one effectively limits the number of accessible RE channels as shown in Fig. 2(b). Squeezing the same number of photons into a 7-fs SASE pulse, as shown in panel (c) of Fig. 2, indicates that the ANREE in a 7-fs pulse tends to be lower than those for the 80-fs pulse. The higher-intensity 7-fs pulse has a higher probability to beat Auger decay and thus favors creation of transients with multiple core holes or hollow core shells which are removed from the resonance condition.

C. 3c: Seeded vs SASE pulses: ultraefficient ionization mechanisms

In Fig. 3 we display $Q_{avg}(SASE) - Q_{avg}(seeded)$ obtained from an 80-fs pulse as a function of PE and ω_X. In general SASE pulses yield a higher average charge state than the seeded pulses, but the degree of enhancement in Q_{avg} does not correlate with ANREE. For example, a 2.5-keV, 75-mJ SASE pulse undergoes >7 RE events to produce an enhancement of only 3 charge states in Q_{avg}, whereas a 1.6-keV, 0.75 mJ SASE pulse undergoes 5 RE events to give the largest enhancement of > 5 charge states.

We examine the origin of this hot spot for ultraefficient resonance-mediated ionization at 1.6 keV in Kr, as shown in Fig.4. At 1.6 keV, the incoming photon cannot excite a 2p electron in neutral Kr via a direct single-photon process. However, Kr^+ with a 2p core hole can be created through a 2-photon process: ionization of 3d shell followed by $2p \rightarrow 3d$ RE. This is analogous to the mechanism first described in Kanter *et al.* for 1s-2p excitation [35], where the first part of the pulse "unveils" the hidden 1s-2p resonance in neon. Due to the relatively large BW, a series of REs $2p \rightarrow 3d$ coupled with inner-shell relaxation to refill the 2p hole, is found to remain on resonance across many charge states from 1+ to 11+. This leads to efficient production of Kr^{13+}, as shown in Fig. 4 (b). This mechanism of core-to-core REs involving short-lived transients followed by Auger decay differs from that involved in producing Ar^{11+}, which invokes long-lived Rydberg ion states [19].

The situation is markedly different in an 80-fs seeded pulse, where the Kr^{9+} is the most probable charge state because the L shell remains transparent, Fig. 4 (b,d,e). Unlike the SASE pulse, where L-shell Auger cascades dominate, the seeded pulse pathways to Kr^{13+} have fewer Auger events because M-shell ionization dominates.

In addition to its strong dependence on bandwidth,

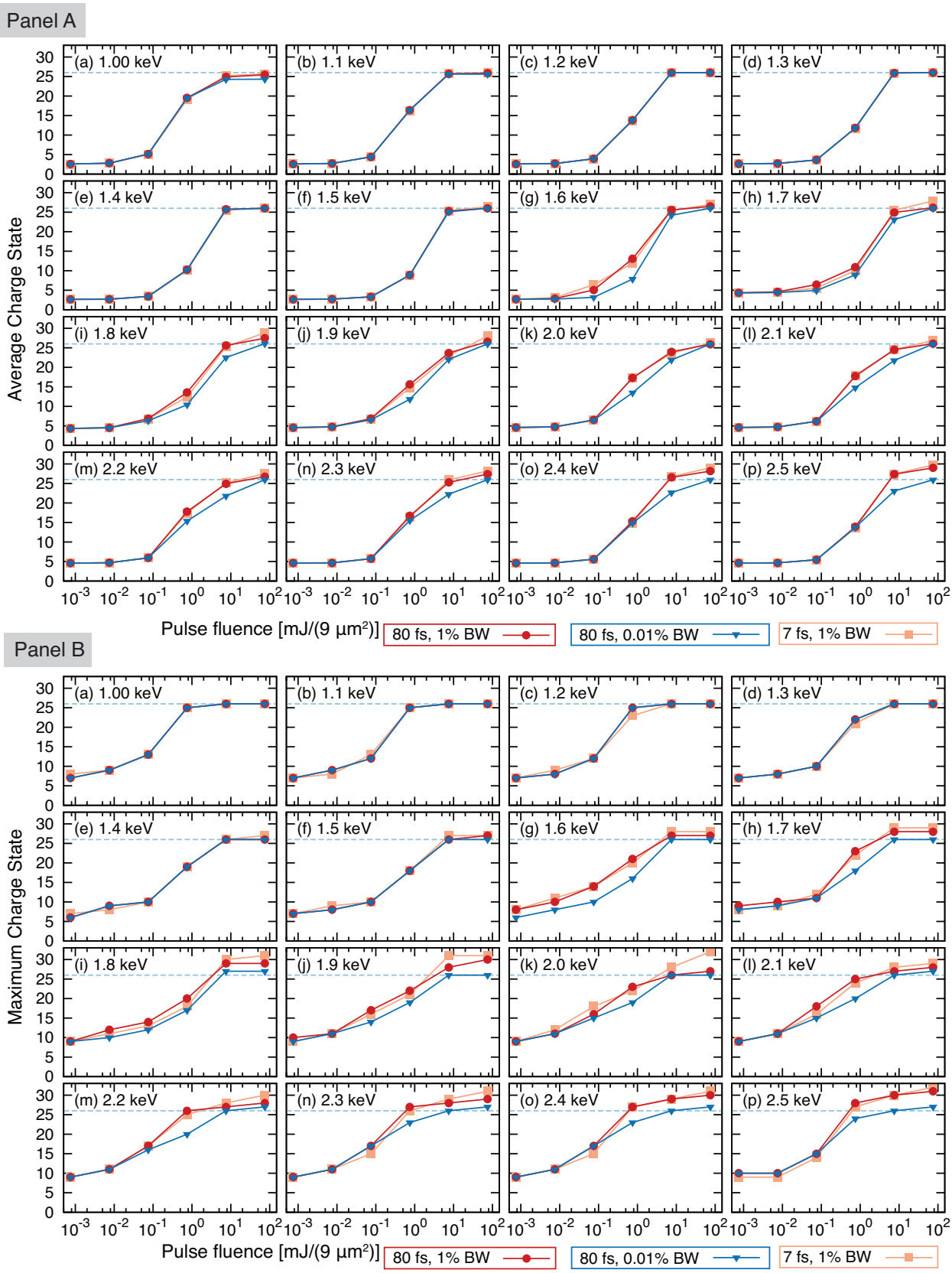

FIG. 5. (Color online) Average charge state (Panel A) and maximum charge state with ion yield larger than 0.01% (Panel B) produced in Kr atom exposed to a seeded pulse (0.01% bandwidth) as a function of x-ray photon energies and pulse energy (or fluence) with an x-ray focus of 9 μm^2. Dashed lines show Kr^{26+} a Ne-like Kr ion.

the Kr ionization dynamics in a 1.6 keV XFEL pulse is also sensitive to pulse duration. A 7-fs SASE pulse favors the creation of transients with multiple L-shell vacancies which are far from the resonance energy condition, and it produces 12+ and above with fewer REs and Auger events than in 80-fs pulse as illustrated in panels (b) to (e) of Fig. 4. Kr ion yields for charge states above 12+ in the 7-fs pulse are smaller than those in the 80-fs pulse, as expected from intensity induced x-ray transparency [3], where refilling the core hole for further photoionization is more probable with longer pulses.

D. 3d: Below-threshold ionization via Preservation of Inner-shell Vacancy

Apart from this hot spot at 1.6 keV, we also reveal more subtle effects in Q_{avg} that depend sensitively on pulse parameters, Fig. 3. Panel A of Fig. 5 shows the average charge state calculated for three types of pulses: 80-fs SASE pulse, 80-fs seeded pulse and 7-fs SASE pulse.

We highlight two observations. First, Q_{avg} from the seeded pulses does not exceed 26+ (25+) for $\omega_X \geq 1.2$ keV ($\omega_X < 1.2$ keV). These maximum Q_{avg} values reflect the sequential single photon limits (boundaries of below-threshold ionization) of ω_X. The ionization potentials (IP) of Kr^{26+} (Ne-like Kr) and Kr^{25+} are 2.92 keV and 1.19 keV respectively. Second, the Q_{avg} enhancement profile as a function of PE depends strongly on ω_X. For most ω_X, the enhancement in 80-fs SASE pulse is found at intermediate PEs, but diminishes at high PEs, corresponding to a plateau Q_{avg} 26+ for the seeded pulses. The seeded v SASE curves form an "eye-opening" shape. Exceptions are found at $\omega_X = 1.0$ keV, 1.8 keV and $\omega_X > 2.2$ keV, where REs are activated near Kr^{26+} and above to produce Q_{avg} as large as 29+ in a 2.5-keV, SASE pulse and go beyond the seeded pulse limit.

The data illustrates that, without nearby REs, below-threshold ionization is not favorable. This is because the potential pathways involve preservation of inner-shell vacancies (PISV) created via RE or direct photoionization at low charge states while the ion undergoes further ionization of electrons in valence/outer shells. This PISV mechanism is not efficient, except in a shorter, more intense pulse that can compete with or overcome the rapid inner-shell relaxation processes. This new pulse duration effect, opposite to trends previously noted from the intensity induced x-ray transparency, gives slightly higher Q_{avg} in 7-fs pulse in the regime of below-threshold ionization.

We find that PISV is the dominant mechanism to produce the highest charge states (see panel B of Fig. 5), particularly beyond Kr^{26+}. This mechanism enables production of Kr^{27+} in a 7-fs, 1.4 keV pulse by preserving a $2p$ hole created in Kr^{+} via RE for more than 20 charge states. PISV also allows a seeded 80-fs pulses to reach $Q_{max} > 26+$. A more extreme example is found in the Kr ionization pathway by the 2.0 keV, 7-fs SASE pulse with the highest PE, where the pulse can produce Kr^{32+}. This production in the 7-fs pulse is the result of being able to access additional L-shell RE windows available at charge states $> 27+$. The 80-fs pulse with the same pulse energy produces only $Q_{max} = 27$ as the longer pulse is less likely to preserve more than one L-shell vacancy.

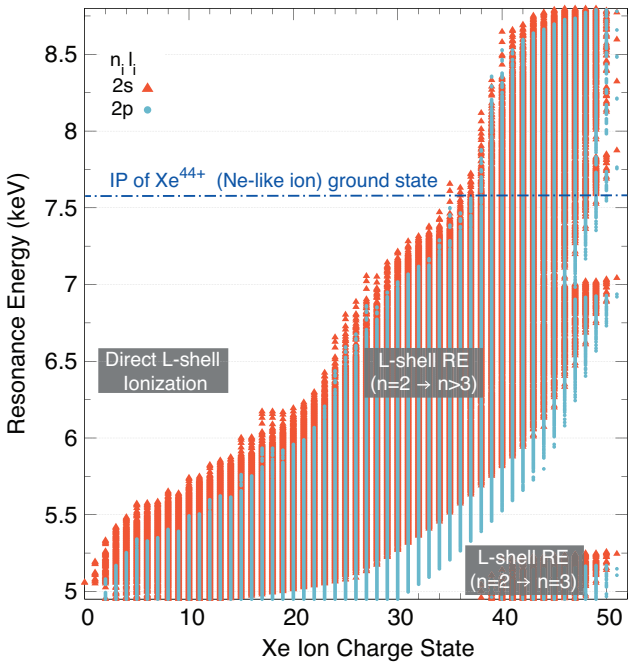

FIG. 6. (Color online) The hidden resonances originated from the 2s (red triangles) or 2p (blue circles) subshell in various charge states of Xe that can be uncovered by a range of incoming x-ray photon energies.

IV. SECTION 4: XE IONIZATION DYNAMICS

We investigated the ionization dynamics of Xe atoms exposed to SASE (1% BW) and seeded (0.01% BW) XFEL pulses with a pulse duration of 45 fs and a focus of 0.1 μm^2 at 16 different photon energies (5 to 8.75 keV) and 9 different pulse energies (0.01 mJ, 0.03 mJ, 0.06 mJ, 0.1 mJ, 0.3 mJ, 0.6 mJ, 1 mJ, 3 mJ, 6 mJ), corresponding roughly to parameters in a recent LCLS experimental run. The photon fluence range is 0.1 to 60 mJ/μm^2. At 5.0 (8.75) keV, the photon number range is 1.25×10^{10} to 7.49×10^{12} (1.73×10^{9} to 4.28×10^{12}) per pulse. The pulse parameters covered by our calculations are within reach at current XFEL facilities.

Fig. 6 shows that RE channels in the range 5 – 8.75 keV originate from either $2s$ or $2p$ initial states. For XFEL pulses with ω_X less than 5.5 keV, the window of RE channels starts at low charge states and extends to 40+. Above 5.5 keV, the start of the RE window is shifted to a higher charge state gradually and the range shrinks as the photon energy increases. For example,

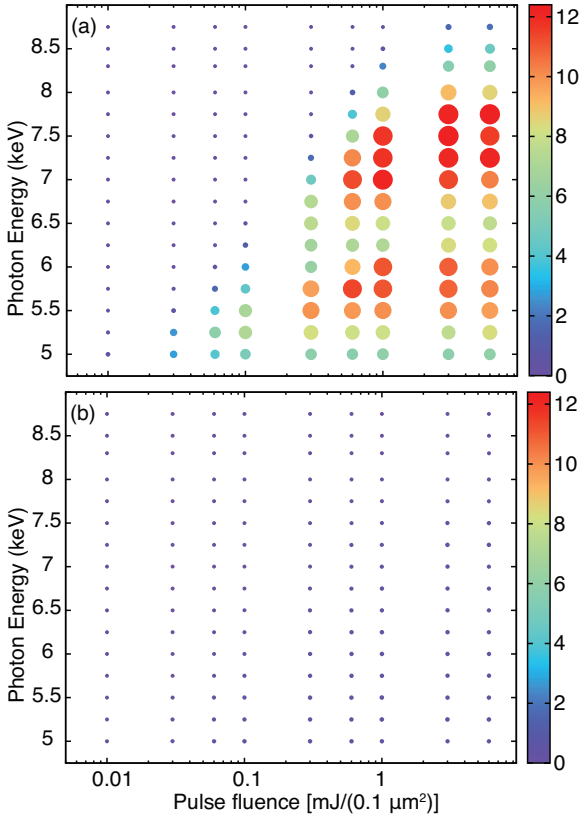

FIG. 7. (Color online) Average number of resonant excitation events occurred in producing a xenon ion in (a) an 80-fs, 1% energy bandwidth XFEL pulse, (b) an 80-fs, 0.01% energy bandwidth XFEL pulse as a function of x-ray photon energies and pulse energy (or fluence) with an x-ray focus of 0.1 μm^2 and pulse duration of 45 fs.

at 6.5 keV, RE channels are found in the range of 25+ to 48+ while at 8.5 keV, RE channels appear only from 45+ to 48+. These localized regions of RE channels have immediate impact on the ionization dynamics. Although the atomic structure of Xe is more complicated than Kr, with 54 electrons and 11 occupied subshells in neutral Xe, we identified similar dynamical signatures due to L-shell resonances.

For the seeded and SASE pulses, we present the ANREE map in Fig. 7, Q_{avg} and Q_{max} in Fig. 8 and the difference signal between the Q_{avg} in Fig. 9. We first list features in Xe that also appear in Kr. The resonance energy landscape of RE channels has direct impact on ANREE as a function of PE and ω_X (see Fig. 7). At 5 keV, the range of PE with ANREE > 2 begins at low PE due to the presence of RE channels at low charges, whereas at 8.75 keV the value of ANREE is less than 1 even at PE of 6 mJ because the available RE channels are hidden at very high charge states. Among all the pulse parameter sets, a 7.75-keV, 6-mJ SASE can initiate the highest number of RE processes, which is about 12. With a seeded pulse, the number RE processes is suppressed to less than 1 for all pulse parameters.

We compare Q_{avg} from SASE and seeded pulses in Fig. 8. In general, The Q_{avg} from the SASE pulse is larger than that from the seeded pulse, but depends strongly on PE and ω_X. As in Kr, an "eye-opening" shape appears starting at 5.0 keV and the shape shifts to higher PE as ω_X increases to 5.75 keV. This shift is a result of the resonance landscape, where higher ω_X only accesses RE channels in higher ion charge states thus requiring higher PE.

The "eye-opening" shape indicates a significant enhancement in Q_{avg} for SASE over the seeded pulses in the intermediate PE range that vanishes at the highest PEs. At the PE where the enhancement vanishes for ω_X <5.75 keV, Q_{avg} reaches a plateau value of 44. Xe^{44+} is a Ne-like ion, such that an L-shell vacancy must be created to exceed this plateau. The ionization potential of ground state Xe^{44+} is 7.6 keV, thus $\omega_X < 7.6$ keV falls in the regime of below threshold ionization. The responsible pathways involve preservation of L-shell vacancies, analogous to the PISV mechanism found for production of Kr^{27+}.

Above 5.5 keV, $Q_{avg} = 44$ no longer serves as a plateau for SASE pulse. This is because resonances are available near Xe^{44+} and beyond, such that a high PE SASE pulse can use these resonances to reach charge states above 44+ without PISV. This is analogous to Kr in a 2.5-keV SASE pulse, where an L-shell RE window reaching Kr^{29+} facilitates production of Kr^{27+} and above. For photon energies ≥7.75 keV, even a high PE seeded pulse can produce charge states above 44+. For this high ω_X range, a new plateau is found at 52, He-like Xe, which is the largest Q_{max} obtained for Xe. Here the K shell is transparent for the ω_X considered.

As in Kr, Q_{avg} enhancement shown in Fig. 9 does not correlate with ANREE. A 5.25-keV SASE pulse with 0.1 mJ represents a hot spot for ultra-efficient ionization via RE. An enhancement of more than 10 charge states in Q_{avg} is obtained with less than 6 RE events. Unlike the hot spot found in Kr, at this Xe hot spot, a broadband SASE pulse activates a series of three types of REs: core-to-outer/Rydberg ($n = 2 \rightarrow n \geq 6$), core-to-valence ($n = 2 \rightarrow n = 5$) and core-to-core ($n = 2 \rightarrow n = 4$) across Xe^{6+} to Xe^{36+}. The availability of these REs at low charge states (<10+) combined with the large ion charge-state RE windows is responsible for the efficiency of these Xe resonant-mediated ionization pathways.

V. SECTION 5: SUMMARY

We presented an efficient numerical scheme to include bound-bound excitations in an MCRE method to track electronic configurations in complex atoms in the presence of XFEL radiation. The search-based database methodology is explained for the first time. We further investigated the impact of bandwidth (seeded: 0.01 % bandwidth vs SASE: 1 % bandwidth) and pulse duration

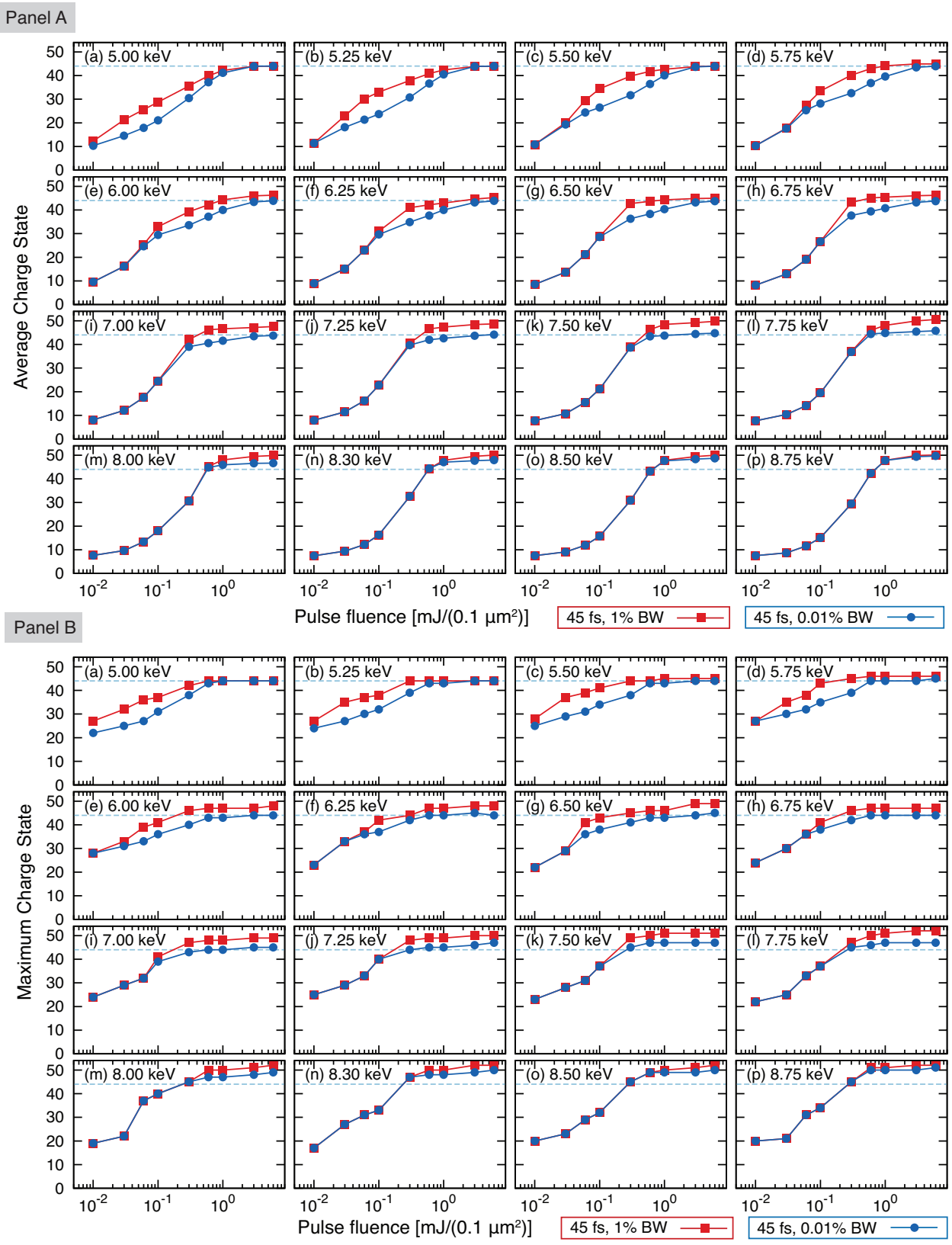

FIG. 8. (Color online) Average charge state (Panel A) and maximum charge state with ion yield larger than 0.01% (Panel B) produced in a Xe atom exposed to SASE (1% bandwidth) and seeded (0.01% bandwidth) pulses as a function of x-ray photon energies and pulse energy (or fluence) with an x-ray focus of 0.1 μm^2 and pulse duration of 45 fs. The dashed line shows Xe^{44+}, a Ne-like Xe ion.

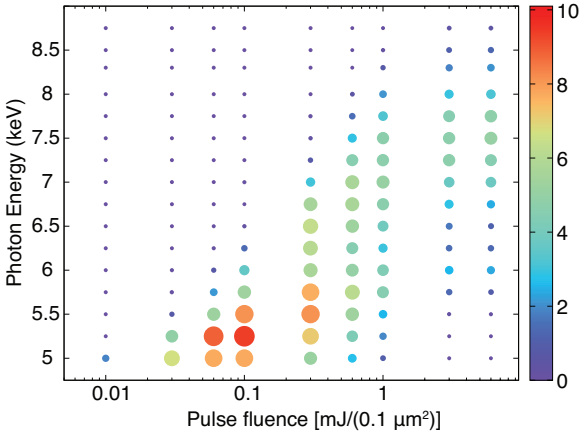

FIG. 9. (Color online) The difference signals between the average charge state of Xe ions exposed to a SASE pulse (1% BW) and a seeded pulse (0.01% BW) as a function of x-ray photon energies and pulse energy (or fluence) with with an x-ray focus of 0.1 μm^2 and pulse duration of 45 fs.

on the atomic ionization dynamics in Kr and Xe over a range of pulse parameters (pulse energy, x-ray photon energy and pulse duration) accessible at current or future XFEL facilities.

The intricate landscape of the resonances is shown to be responsible for the pulse parameter dependence found in Kr and Xe. The photon energy defines a range of ion charge state windows where resonance excitations are possible. A higher fluence is needed to access resonances hidden at higher charge states. We confirm the intuitive notion that a seeded pulse leads to suppression of resonance excitations in the multi-photon ionization pathways of Kr and Xe. We further show that a short pulse suppresses REs as it favors creation of multiple core-hole transients that are away from resonance.

Hot spots with a maximal difference between seeded and SASE pulses are found for both Kr and Xe. In Kr atoms at 1.6-keV a 80-fs SASE pulse with an 0.083 mJ/μm^2 (10^{12} photons/pulse), can initiate ultra-efficient ionization pathways driven by a series of $2p \rightarrow 3d$ (core-to-core) REs from Kr^+ to Kr^{11+} and gives an enhancement of 5 charge states in average charge state over that in a seeded pulse. In Xe atoms exposed to a 5.25-keV, 45-fs SASE pulse with an intermediate fluence of 1 mJ/μm^2 (10^{11} photons/pulse), rather than in the pulse with 60 times more fluence. Here, unlike for Kr at 1.6 keV, a broadband SASE pulse activates a sequence of three types of REs: core-to-outer/Rydberg, core-to-valence and core-to-core across Xe^{6+} to Xe^{36+} and gives an enhancement of more than 10 charge states in average charge state over that in a seeded pulse.

We also uncovered a pulse duration dependence, opposite to that previously observed and dubbed intensity-induced x-ray transparency or frustrated absorption [3, 20, 58], where a shorter, more intense pulse produces higher charge states. This pulse duration dependence was found in the regime of below-threshold ionization in Kr, where the route to very high charge states requires preservation of the inner-shell vacancy created earlier in the pulse via photoionization or REs and thus requires a shorter/intense pulse.

VI. ACKNOWLEDGMENTS

We thank R. Dunford for his comments on the manuscript and D. Rolles, A. Rudenko, S. Southworth, B. Krässig and C. Bostedt for fruitful discussions. This material is based upon work supported by the U.S. Department of Energy, Office of Science, Office of Basic Energy Sciences, Chemical Sciences, Geosciences, and Biosciences Division under Contract No. DE-AC02-06CH11357.

[1] P. Emma, R. Akre, J. Arthur, R. Bionta, C. Bostedt, J. Bozek, A. Brachmann, P. Bucksbaum, R. Coffee, F.-J. Decker, Y. Ding, D. Dowell, S. Edstrom, J. Fisher, A. Frisch, S. Gilevich, J. Hastings, G. Hays, P. Hering, Z. Huang, R. Iverson, H. Loos, M. Messerschmidt, A. Miahnahri, S. Moeller, H.-D. Nuhn, G. Pile, D. Ratner, J. Rzepiela, D. Schultz, T. Smith, P. Stefan, H. Tompkins, J. Turner, J. Welch, W. White, J. Wu, G. Yocky, and J. Galayda, Nat. Photon. **4**, 641 (2010).

[2] T. Ishikawa, H. Aoyagi, T. Asaka, Y. Asano, N. Azumi, T. Bizen, H. Ego, K. Fukami, T. Fukui, Y. Furukawa, S. Goto, H. Hanaki, T. Hara, T. Hasegawa, T. Hatsui, A. Higashiya, T. Hirono, N. Hosoda, M. Ishii, T. Inagaki, Y. Inubushi, T. Itoga, Y. Joti, M. Kago, T. Kameshima, H. Kimura, Y. Kirihara, A. Kiyomichi, T. Kobayashi, C. Kondo, T. Kudo, H. Maesaka, X. M. Marechal, T. Masuda, S. Matsubara, T. Matsumoto, T. Matsushita, S. Matsui, M. Nagasono, N. Nariyama, H. Ohashi, T. Ohata, T. Ohshima, S. Ono, Y. Otake, C. Saji, T. Sakurai, T. Sato, K. Sawada, T. Seike, K. Shirasawa, T. Sugimoto, S. Suzuki, S. Takahashi, H. Takebe, K. Takeshita, K. Tamasaku, H. Tanaka, R. Tanaka, T. Tanaka, T. Togashi, K. Togawa, A. Tokuhisa, H. Tomizawa, K. Tono, S. Wu, M. Yabashi, M. Yamaga, A. Yamashita, K. Yanagida, C. Zhang, T. Shintake, H. Kitamura, and N. Kumagai, Nat. Photon. **6**, 540 (2012).

[3] L. Young, E. P. Kanter, B. Krässig, A. M. March, S. T. Pratt, R. Santra, S. Southworth, N. Rohringer, L. F. DiMauro, G. Doumy, C. A. Roedig, N. Berrah, L. Fang, M. Hoener, P. H. Bucksbaum, J. P. Cryan, S. Ghimire, J. M. Glownia, D. A. Reis, J. D. Bozek, C. Bostedt, and M. Messerschmidt, Nature **466**, 56 (2010).

[4] L. Fang, M. Hoener, O. Gessner, F. Tarantelli, S. T. Pratt, O. Kornilov, C. Buth, M. Gühr, E. P. Kanter, C. Bostedt, J. D. Bozek, P. H. Bucksbaum, M. Chen, R. Coffee, J. Cryan, M. Glownia, E. Kukk, S. R. Leone, and N. Berrah, Phys. Rev. Lett. **105**, 083005 (2010).

[5] H. Fukuzawa, S.-K. Son, K. Motomura, S. Mondal, K. Nagaya, S. Wada, X.-J. Liu, R. Feifel, T. Tachibana, Y. Ito, M. Kimura, T. Sakai, K. Matsunami, H. Hayashita, J. Kajikawa, P. Johnsson, M. Siano, E. Kukk, B. Rudek, B. Erk, L. Foucar, E. Robert, C. Miron, K. Tono, Y. Inubushi, T. Hatsui, M. Yabashi, M. Yao, R. Santra, and K. Ueda, Phys. Rev. Lett. **110**, 173005 (2013).

[6] B. Rudek, S.-K. Son, L. Foucar, S. W. Epp, B. Erk, R. Hartmann, M. Adolph, R. Andritschke, A. Aquila, N. Berrah, C. Bostedt, J. Bozek, N. Coppola, F. Filsinger, H. Gorke, T. Gorkhover, H. Graafsma, L. Gumprecht, A. Hartmann, G. Hauser, S. Herrmann, H. Hirsemann, P. Holl, A. Homke, L. Journel, C. Kaiser, N. Kimmel, F. Krasniqi, K.-U. Kuhnel, M. Matysek, M. Messerschmidt, D. Miesner, T. Moller, R. Moshammer, K. Nagaya, B. Nilsson, G. Potdevin, D. Pietschner, C. Reich, D. Rupp, G. Schaller, I. Schlichting, C. Schmidt, F. Schopper, S. Schorb, C.-D. Schroter, J. Schulz, M. Simon, H. Soltau, L. Struder, K. Ueda, G. Weidenspointner, R. Santra, J. Ullrich, A. Rudenko, and D. Rolles, Nat Photon **6**, 858 (2012).

[7] B. Rudek, D. Rolles, S.-K. Son, L. Foucar, B. Erk, S. Epp, R. Boll, D. Anielski, C. Bostedt, S. Schorb, R. Coffee, J. Bozek, S. Trippel, T. Marchenko, M. Simon, L. Christensen, S. De, S.-i. Wada, K. Ueda, I. Schlichting, R. Santra, J. Ullrich, and A. Rudenko, Phys. Rev. A **87**, 023413 (2013).

[8] R. Neutze, R. Wouts, D. van der Spoel, E. Weckert, and J. Hajdu, Nature **406**, 752 (2000).

[9] H. N. Chapman, P. Fromme, A. Barty, T. A. White, R. A. Kirian, A. Aquila, M. S. Hunter, J. Schulz, D. P. DePonte, U. Weierstall, R. B. Doak, F. R. N. C. Maia, A. V. Martin, I. Schlichting, L. Lomb, N. Coppola, R. L. Shoeman, S. W. Epp, R. Hartmann, D. Rolles, A. Rudenko, L. Foucar, N. Kimmel, G. Weidenspointner, P. Holl, M. Liang, M. Barthelmess, C. Caleman, S. Boutet, M. J. Bogan, J. Krzywinski, C. Bostedt, S. Bajt, L. Gumprecht, B. Rudek, B. Erk, C. Schmidt, A. Homke, C. Reich, D. Pietschner, L. Struder, G. Hauser, H. Gorke, J. Ullrich, S. Herrmann, G. Schaller, F. Schopper, H. Soltau, K.-U. Kuhnel, M. Messerschmidt, J. D. Bozek, S. P. Hau-Riege, M. Frank, C. Y. Hampton, R. G. Sierra, D. Starodub, G. J. Williams, J. Hajdu, N. Timneanu, M. M. Seibert, J. Andreasson, A. Rocker, O. Jonsson, M. Svenda, S. Stern, K. Nass, R. Andritschke, C.-D. Schroter, F. Krasniqi, M. Bott, K. E. Schmidt, X. Wang, I. Grotjohann, J. M. Holton, T. R. M. Barends, R. Neutze, S. Marchesini, R. Fromme, S. Schorb, D. Rupp, M. Adolph, T. Gorkhover, I. Andersson, H. Hirsemann, G. Potdevin, H. Graafsma, B. Nilsson, and J. C. H. Spence, Nature **470**, 73 (2011).

[10] M. Seibert, T. Ekeberg, F. Maia, M. Svenda, J. Andreasson, O. Jönsson, D. Odić, B. Iwan, A. Rocker, D. Westphal, *et al.*, Nature **470**, 78 (2011).

[11] A. Kondratenko and E. Saldin, Part. Accelerators **10**, 207 (1980).

[12] G. Geloni, V. Kocharyan, and E. Saldin, (2010), arXiv:1012.3617 [physics.acc-ph].

[13] J. Feldhaus, E. L. Saldin, J. R. Schneider, E. A. Schneidmiller, and M. V. Yurkov, Optics Communications **140**, 341 (1997).

[14] J. Amann, W. Berg, V. Blank, F.-J. Decker, Y. Ding, P. Emma, Y. Feng, J. Frisch, D. Fritz, J. Hastings, Z. Huang, J. Krzywinski, R. Lindberg, H. Loos, A. Lutman, H.-D. Nuhn, D. Ratner, J. Rzepiela, D. Shu, Y. Shvyd'ko, S. Spampinati, S. Stoupin, S. Terentyev, E. Trakhtenberg, D. Walz, J. Welch, J. Wu, A. Zholents, and D. Zhu, Nat. Photon. **6**, 693 (2012).

[15] D. Ratner, R. Abela, J. Amann, C. Behrens, D. Bohler, G. Bouchard, C. Bostedt, M. Boyes, K. Chow, D. Cocco, F. J. Decker, Y. Ding, C. Eckman, P. Emma, D. Fairley, Y. Feng, C. Field, U. Flechsig, G. Gassner, J. Hastings, P. Heimann, Z. Huang, N. Kelez, J. Krzywinski, H. Loos, A. Lutman, A. Marinelli, G. Marcus, T. Maxwell, P. Montanez, S. Moeller, D. Morton, H. D. Nuhn, N. Rodes, W. Schlotter, S. Serkez, T. Stevens, J. Turner, D. Walz, J. Welch, and J. Wu, Phys. Rev. Lett. **114**, 054801 (2015).

[16] S. Serkez, V. Kocharyan, E. Saldin, I. Zagorodnov, and G. Geloni, Proceedings of FEL2014, Basel, Switzerland, MOP057.

[17] A. A. Lutman, R. Coffee, Y. Ding, Z. Huang, J. Krzywinski, T. Maxwell, M. Messerschmidt, and H.-D. Nuhn, Phys. Rev. Lett. **110**, 134801 (2013).

[18] A. Marinelli, D. Ratner, A. A. Lutman, J. Turner, J. Welch, F. J. Decker, H. Loos, C. Behrens, S. Gilevich, A. A. Miahnahri, S. Vetter, T. J. Maxwell, Y. Ding, R. Coffee, S. Wakatsuki, and Z. Huang, Nat Commun **6**, 6369 (2015).

[19] P. J. Ho, C. Bostedt, S. Schorb, and L. Young, Phys. Rev. Lett. **113**, 253001 (2014).

[20] S. Schorb, D. Rupp, M. L. Swiggers, R. N. Coffee, M. Messerschmidt, G. Williams, J. D. Bozek, S.-I. Wada, O. Kornilov, T. Möller, and C. Bostedt, Phys. Rev. Lett. **108**, 233401 (2012).

[21] S. Schorb, Ph. D. Thesis, Technischen Universität Berlin (2012).

[22] S.-K. Son and R. Santra, XATOM – an integrated toolkit for X-ray and atomic physics, Rev. 304 (CFEL, DESY, 2011).

[23] S.-K. Son, L. Young, and R. Santra, Phys. Rev. A **83**, 033402 (2011).

[24] S.-K. Son and R. Santra, Phys. Rev. A **85**, 063415 (2012).

[25] T. Mukoyama, Bull. Inst. Chem. Res. Kyoto Univ. **63**, 373 (1985).

[26] M. N. Mirakhmedov and E. S. Parilis, J. Phys. B: At. Mol. Opt. Phys. **21**, 795 (1988).

[27] M. Opendak, Astrophys. Space Sci. **165**, 9 (1990).

[28] A. El-Shemi, Y. Lofty, and G. Zschornack, J. Phys. B: At. Mol. Opt. Phys. **30**, 237 (1997).

[29] A. M. El-Shemi, A. A. Ghoneim, and Y. A. Lotfy, Turk. J. Phys **27**, 51 (2003).

[30] A. H. Abdullah, A. M. El-Shemi, and A. A. Ghoneim, Rad. Phys. and Chem. **68**, 697 (2003).

[31] K. Motomura, H. Fukuzawa, S.-K. Son, S. Mondal, T. Tachibana, Y. Ito, M. Kimura, K. Nagaya, T. Sakai, K. Matsunami, S. Wada, H. Hayashita, J. Kajikawa, X.-J. Liu, R. Feifel, P. Johnsson, M. Siano, E. Kukk, B. Rudek, B. Erk, L. Foucar, E. Robert, C. Miron, K. Tono, Y. Inubushi, T. Hatsui, M. Yabashi, M. Yao, R. Santra, and K. Ueda, J. Phys. B: At. Mol. Opt. Phys. **46**, 164024 (2013).

[32] N. Rohringer and R. Santra, Phys. Rev. A **76**, 033416 (2007).

[33] G. Doumy, C. Roedig, S.-K. Son, C. I. Blaga, A. D. DiChiara, R. Santra, N. Berrah, C. Bostedt, J. D. Bozek, P. H. Bucksbaum, J. P. Cryan, L. Fang, S. Ghimire, J. M. Glownia, M. Hoener, E. P. Kanter, B. Krässig, M. Kuebel, M. Messerschmidt, G. G. Paulus, D. A. Reis, N. Rohringer, L. Young, P. Agostini, and L. F. DiMauro, Phys. Rev. Lett. **106**, 083002 (2011).

[34] A. Sytcheva, S. Pabst, S.-K. Son, and R. Santra, Phys. Rev. A **85**, 023414 (2012).

[35] E. P. Kanter, B. Krässig, Y. Li, A. M. March, P. Ho, N. Rohringer, R. Santra, S. H. Southworth, L. F. DiMauro, G. Doumy, C. A. Roedig, N. Berrah, L. Fang, M. Hoener, P. H. Bucksbaum, S. Ghimire, D. A. Reis, J. D. Bozek, C. Bostedt, M. Messerschmidt, and L. Young, Phys. Rev. Lett. **107**, 233001 (2011).

[36] N. Rohringer and R. Santra, Phys. Rev. A **76**, 033416 (2007).

[37] Consider an atom with N active/accessible orbitals and g_j is the maximum occupation number of the active orbital j. Let C_k be the number of EC with a total number of k electrons in all active orbitals. In fact, C_k is the partition function for partitioning the integer k into N integers. In number theory, the generating function of C_k is given by

$$\sum_k C_k x^k = (1-x)^{-N} \prod_{j=1}^{N} (1 - x^{g_j+1}). \tag{5}$$

Then the total number of ECs with k_i to k_f electrons is given by $\sum_{k=k_i}^{k=k_f} C_k$.

[38] J. C. Slater, Phys. Rev. **81**, 385 (1951).

[39] F. Herman and S. Skillman, *Atomic structure calculations* (Prentice-Hall, Englewood Cliffs, New Jersey, 1963).

[40] C. P. Bhalla, N. O. Folland, and M. A. Hein, Phys. Rev. A **8**, 649 (1973).

[41] P. Auger, J. Phys. Radium **6**, 205 (1925).

[42] D. Coster and R. Kronig, Physica **2**, 13 (1935).

[43] A. T. Kiang, S. T. Ma, and T.-Y. Wu, Phys. Rev. **50**, 673 (1936).

[44] J. W. Cooper, Phys. Rev. **128**, 681 (1962).

[45] S. T. Manson and J. W. Cooper, Phys. Rev. **165**, 126 (1968).

[46] B. F. Rozsnyai, Journal of Quantitative Spectroscopy and Radiative Transfer **15**, 695 (1975).

[47] I. I. Sobelman, *Introduction to The Theory of Atomic Spectra*, International Series in Natural Philosophy, Vol. 40 (Springer, Berlin, 1974).

[48] E. McGuire, in *Atomic Inner-Shell Processes*, edited by B. Crasemann (Academic Press, 1975) pp. 293 – 330.

[49] R. C. Hilborn, Am. J. Phys. **50**, 982 (1982).

[50] M. J. Seaton and G. Peach, Proceedings of the Physical Society **79**, 1296 (1962).

[51] J.-J. Yeh and I. Lindau, At. Data Nucl. Data Tables **32**, 1 (1985).

[52] J. Boyd, *Chebyshev and Fourier Spectral Methods: Second Revised Edition*, Dover Books on Mathematics (Dover Publications, 2001).

[53] J. Y. Wang, S. I. Chu, and C. Laughlin, Phys. Rev. A **50**, 3208 (1994).

[54] G. H. Yao and S. I. Chu, Chem. Phys. Lett. **204**, 381 (1993).

[55] V. Szalay, J. Chem. Phys. **99**, 1978 (1993).

[56] L. Greenman, P. J. Ho, S. Pabst, E. Kamarchik, D. A. Mazziotti, and R. Santra, Phys. Rev. A **82**, 023406 (2010).

[57] H. Mimura, H. Yumoto, S. Matsuyama, T. Koyama, K. Tono, Y. Inubushi, T. Togashi, T. Sato, J. Kim, R. Fukui, Y. Sano, M. Yabashi, H. Ohashi, T. Ishikawa, and K. Yamauchi, Nat Commun **5**, 3539 (2014).

[58] M. Hoener, L. Fang, O. Kornilov, O. Gessner, S. T. Pratt, M. Gühr, E. P. Kanter, C. Blaga, C. Bostedt, J. D. Bozek, P. H. Bucksbaum, C. Buth, M. Chen, R. Coffee, J. Cryan, L. DiMauro, M. Glownia, E. Hosler, E. Kukk, S. R. Leone, B. McFarland, M. Messerschmidt, B. Murphy, V. Petrovic, D. Rolles, and N. Berrah, Phys. Rev. Lett. **104**, 253002 (2010).